Additive Manufacturing 39 (2021) 101880

Contents lists available at ScienceDirect

Additive Manufacturing

journal homepage: www.elsevier.com/locate/addma

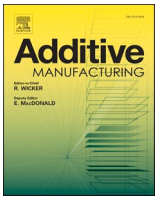

Laser powder bed fusion of soda lime silica glass: Optimisation of processing parameters and evaluation of part properties

K.C. Datsiou [a,1], F. Spirrett [a], I. Ashcroft [a], M. Magallanes [b], S. Christie [c], R. Goodridge [a,*]

[a] Centre for Additive Manufacturing, University of Nottingham, Nottingham NG8 1BB, UK
[b] Glass Technology Services, Sheffield S35 2PY, UK
[c] School of Chemistry, Loughborough University, Loughborough LE11 3TU, UK

ARTICLE INFO

Keywords:
Laser powder bed fusion
Additive manufacturing
Glass
Property characterisation

ABSTRACT

Glass has a number of attractive properties, such as transparency, chemical resistance, good thermal stability and high electrical resistivity, that make it a favourable material for a range of applications, including medical technology, electronics, chemical and pharmaceutical industries. However, compared to metals and polymers, the additive manufacturing of glass is still at a primitive stage. The inherent material properties of glass, i.e. its amorphous structure, lack of ductility and high processing temperatures, make processing of glass by additive manufacturing challenging. This paper describes the laser powder bed fusion of a soda lime silica glass. Optimisation of the laser powder bed fusion process was undertaken and the physical and mechanical properties of the manufactured parts were characterised revealing an average porosity of 12%, a mean flexural strength of 6.5 MPa and a fully amorphous structure. Feasibility examples were successfully demonstrated, indicating that geometrically complex shapes are possible. Even though the manufactured parts are opaque, they could potentially find use in applications where the need for chemical inertness and geometrical complexity surpass the need for transparency as in the chemical and pharmaceutical industries e.g. in the form of continuous flow reactors or structured catalysts.

1. Introduction

Glass, which is made from natural and plentiful raw materials, has a unique set of physical properties including light transmission, transparency, chemical durability (with caustic solutions being the common exception), thermal stability and electric resistivity. These properties make glass attractive to a wide range of industries from the architectural, automotive and aerospace industries to the electronics, packaging, chemical manufacturing and pharmaceutical industries. Currently, complex shapes of glass are created with the use of moulds e.g. in glass casting and pressing or glass hot bending that is typically used in the architectural or automotive industries, where a flat sheet of glass is heated above its transition temperature while gravity forces it to take the shape of a mould beneath the glass. Separate moulds are required for different glass geometries, increasing costs and embodied carbon in these production processes. Subtractive methods such as laser ablation or micro-machining are used in the chemical manufacturing, pharmaceutical and electronics industries for complex glass geometries. However, these require long lead times, limit customization and result in material waste. The development of a successful Additive Manufacturing (AM) method to process glass could address these limitations, allowing more complex glass objects to be produced, in a reproducible and cost-effective way, particularly for prototyping or limited production volumes.

A variety of AM methods have been investigated for glass to date, including stereolithography [1], direct ink writing [2,3], fused deposition modelling [4,5], laser powder bed fusion [6,7]. However, each of them comes with their own strengths and limitations in terms of resolution, geometric accuracy and optical quality. Indirect methods (stereolithography [1] and direct ink writing [2,3]) offer transparency, however, compromise geometric accuracy due to the volumetric, often anisotropic, shrinkage arising from post-manufacturing heat treatment needed to remove organic content and sintering to densify the parts. Fused deposition modelling [4,5] is a direct method, however, it is limited in resolution which is dictated by the geometry and dimensions of the nozzle in use. Laser powder bed fusion (LPBF) [6,7] addresses the

* Corresponding author.
E-mail address: ruth.goodridge@nottingham.ac.uk (R. Goodridge).
[1] Present address: Eckersley O'Callaghan, London WC1X 8HB, UK

https://doi.org/10.1016/j.addma.2021.101880
Received 18 September 2020; Received in revised form 3 January 2021; Accepted 29 January 2021
Available online 3 February 2021

above limitations, however, results in opaque, non-transparent parts.

This paper draws upon the knowledge and conclusions of our short communication paper [6], providing a more detailed description and demonstrating the capabilities of the developed laser powder bed fusion process for glass. Additionally, it evaluates the physical and mechanical properties of the built parts and proposes potential uses of the technology. In particular, Sections 2 and 3 describe the feedstock material and the manufacturing method respectively, while Section 4 provides feasibility examples and potential uses of the developed technology in the chemical manufacturing industry. Section 5 provides an overview of the methods used for the assessment of the physical (geometrical accuracy, porosity, crystallinity) and mechanical properties of the produced parts. Finally, Section 6 presents and discusses property results of the produced parts whilst Section 7 summarizes important results and conclusions.

2. Materials

Two soda lime silica glass powders named SLSG109 and SLSG44 in this study, were used as feedstock material. The two feedstock materials had largely identical compositions (available in Table 1 as determined by EDX - JEOL 6060LV SEM, USA), and only differed in terms of particle size to assess its influence on glass processing with LPBF.

Laser diffraction (Malvern, Mastersizer 3000, UK) revealed a Gaussian particle size distribution for both powders (Fig. 1) with an average particle size of 109 μm and 44 μm for SLSG109 and SLSG44 respectively. The wider Gaussian distribution for SLSG44 suggests a better packing density as the larger amount of fine particles reduces inter-particle voids. Relatively fine powders with high packing density are generally preferred in LPBF as they provide a larger surface area for laser processing (22.8 m^2/kg for SLSG109 against 58.3 m^2/kg for SLSG44) and minimize porosity in the built parts; however, too fine a powder can cause difficulties with flow, deposition and spreading of the powder over the build area [8].

The feedstock material comprised spherical particles for both powders (insets available in Fig. 1). Spherical particles improve flowability and therefore powder deposition in LPBF [9]. The flowability of both feedstock materials was assessed with a FT4 Powder Rheometer (Freeman technology, USA). The basic flowability energy, *BFE*, i.e. the energy required (torque and axial force) for the blade to move through the sample at a rate of 100 mm/s, was found to be higher for SLSG44 (*BFE*=168 mJ) compared to SLSG109 (*BFE* = 146 mJ) indicating poorer flowability for the former (Fig. 2). Additionally, the flow rate index, *FRI*, i.e. the ratio of the flow energies at 10 mm/s over 100 mm/s was measured to determine any cohesiveness in the feedstock. Cohesive powders (*FRI* > 1) are sensitive to modifications in the flow rate of the blade as it moves through the sample. A *FRI* of 1.22 and 1.08 were found for SLSG44 and SLSG109 respectively, denoting a slightly cohesive behaviour for SLSG44. The poorer flowability performance of SLSG44 compared to SLSG109 could be attributed to its smaller particle size with inter-particle forces possibly increasing and inhibiting flowability.

Differential scanning calorimetry (Q600–TA Instruments, USA) indicated very similar transition and melting temperatures for both samples, at about 575 °C and 1280 °C respectively.

Table 1
Chemical composition of glass feedstock by weight from electron microscopy for: (a) elements and (b) oxides.

(a) Elements % Weight								
Sample	Na	Mg	Al	Si	K	Ca	O	Total
SLSG109	10.5	2.1	0.3	33.8	0.2	6.5	46.5	100.0
SLSSG44	10.2	1.5	0.6	33.7	0.4	7.3	46.4	100.0
(b) Oxides % Weight								
Sample	Na	Mg	Al	Si	K	Ca	Total	
SLSG109	14.2	3.5	0.5	72.4	0.3	9.1	100.0	
SLSG44	13.7	2.5	1.1	72.1	0.5	10.2	100.0	

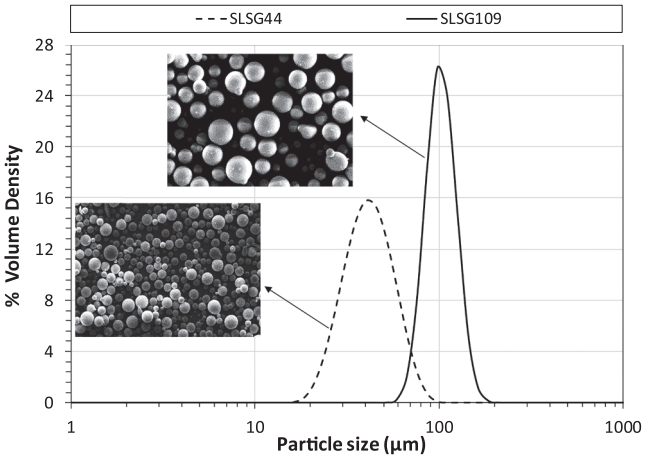

Fig. 1. Particle size distribution and SEM micrographs at 200x magnification for both glass feedstock.

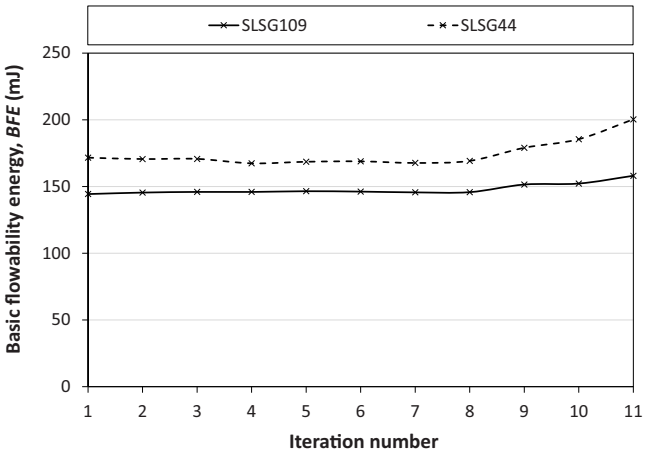

Fig. 2. Basic flowability energy for the selected glass feedstock.

3. Manufacturing method

This section describes the LPBF process and the optimisation steps for the processing parameters. Single tracks were used as a first step, in Section 3.1, to assess powder consolidation and inform the selection of substrate. These findings formed the basis for investigating the interaction between neighbouring layers in thin walled structures (manufactured by a linear laser scan repeated over multiple layers) whilst identifying their processing window in Section 3.2. These in turn provided insight on wall resolution that was eventually used to inform the hatch spacing between adjacent melt tracks for the formation of hatched, multilayer, cubic structures in Section 3.2.

3.1. Laser powder bed fusion

The LPBF approach in this study employed a commercial system (ReaLizer GmbH SLM-50, Germany) to process the selected glass feedstock. SLM-50 uses an yttrium fibre laser operating at a wavelength of 1064 nm. The feedstock material was deposited in layers of uniform thickness through an automated wiper system on a 70 mm diameter platform. The layer thickness was selected to accommodate the largest particle size in the feedstock, which was 70 μm for SLSG44 and 120 μm for SLSG109. The temperature of the platform was maintained at 250 °C during the manufacturing process through an integrated heater to

reduce the temperature gradients developed through the thickness of the built part. If oxygen levels increased above the threshold of 0.9%, argon flow at 1000Lt per min ensured inert conditions and prevented oxidation. A focus position of 9.6 mm was selected in this study. This is the distance between the laser diode and the lens and determines the diameter spot size, which in this case corresponded to 20 μm.

Similar compositions for substrate and feedstock material are typically selected in LPBF to achieve adhesion and accommodate thermal expansion. However, this study revealed limitations when a 1 mm thick, soda lime silica glass substrate was used over the standard SLM-50 titanium platform for the LPBF of glass as etching was observed on the lower surface of the glass substrate (Fig. 3a).

The low absorptivity of the glass feedstock and the glass substrate resulted in part of the laser irradiation reaching the surface of the titanium base plate underneath the glass substrate. Part of this irradiation was subsequently reflected and re-directed to the glass substrate, etching its lower surface (Fig. 3a). Etching could be prevented by fixing the glass substrate to a less reflective base plate e.g. alumina (Fig. 3b). Single layer designs could be successfully created with this set-up (Fig. 4) opening up the potential for glass decoration applications. However, micro-cracks formed on the glass substrate that could propagate and eventually trigger fracture during the laser processing of subsequent layers in multi-layer parts, causing the build to fail. Alumina substrates have higher thermal resistance than glass and similar coefficients of thermal expansion and can therefore minimize thermal cracking whilst providing adequate adhesion to glass. High purity alumina discs with a thickness of 2.5 mm were therefore selected for subsequent investigation in this study.

3.2. Energy density optimisation

Process maps were developed to identify the optimal processing window for both feedstock materials, calculating the deposited energy density as a function of the processing parameters, in a similar manner to the method described in [6]. A 2D approach was used for thin-walled structures where a single linear laser scan was sufficient per layer (Fig. 5a-b), taking into account laser power, P, scan speed, v, and layer thickness, t, (Eq. 1a) while a 3D approach was followed for parts that involved multiple and adjacent laser scans per layer (Fig. 6a-b), taking also into account the hatch spacing, h, (Eq. 1b).

$$ED_{2D} = P/(v \cdot t) \text{ and } ED_{3D} = P/(v \cdot h \cdot t) \quad \text{(1a-b)}$$

It was found that thin walled structures (Fig. 7a) required at least 27 J/mm^2 and 30 J/mm^2 for SLSG44 and SLSG109 respectively to achieve melting and consolidation of the powder (Fig. 5a-b). Energy densities below this limit resulted in poor consolidation (example shown in Fig. 7a). Thick walled structures required energy densities between

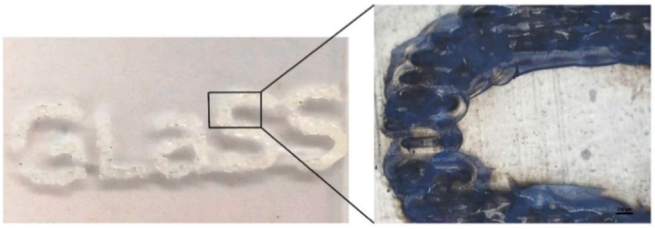

Fig. 4. Example of single layer of laser powder bed fusion of soda lime silica glass on a glass substrate fixed on an alumina plate.

$70 \leq ED_{3D} \leq 120$ J/mm^3 and $65 \leq ED_{3D} \leq 110$ J/mm^3 for SLSG44 and SLSG109 respectively (Fig. 6a-b). Energy densities below this range led to poor consolidation and brittle parts, similar to the thin walled structures at low energy, while energy densities exceeding this range led to balling and therefore excessive track height and poor dimensional accuracy for both feedstock (typical examples shown in Fig. 7b). These process maps can be now used for manufacturing parts irrespective of the level of complexity in design; examples are given in Section 4.

Very similar processing windows were found for thin and thick-walled parts for both feedstock. The effect of energy density was therefore independent of particle size for feedstock of the same composition. However, layer thickness could be reduced when the finer powder was used, e.g. the minimum permissible layer thickness was 70 μm for SLSG44 versus 120 μm for SLSG109, which in turn resulted in higher resolution. Optical microscopy of thin walls (single laser scans repeated per layer, Fig. 7a), confirmed this, revealing that higher resolution i.e. smaller wall thickness, was obtained for SLSG44 compared to SLSG109 for the same energy density (Fig. 8). The smallest feature achievable for the lowest energy density of the optimal processing window was 575 μm for SLSG109 whilst this diminished to 385 μm for SLSG44. For these reasons, parts manufactured with SLSG44 were only subsequently evaluated in this study.

4. Feasibility examples and potential applications

The glass parts manufactured with laser powder bed fusion are opaque as shown in Fig. 7. This is attributed to the presence of superficial, partially fused powder particles and internal defects (discussed in detail in Section 5.2). Even though transparency is desirable, there are applications where the need for geometrical complexity in combination with chemical inertness is more crucial. Such applications can be found in the pharmaceutical and chemical manufacturing industries and include:

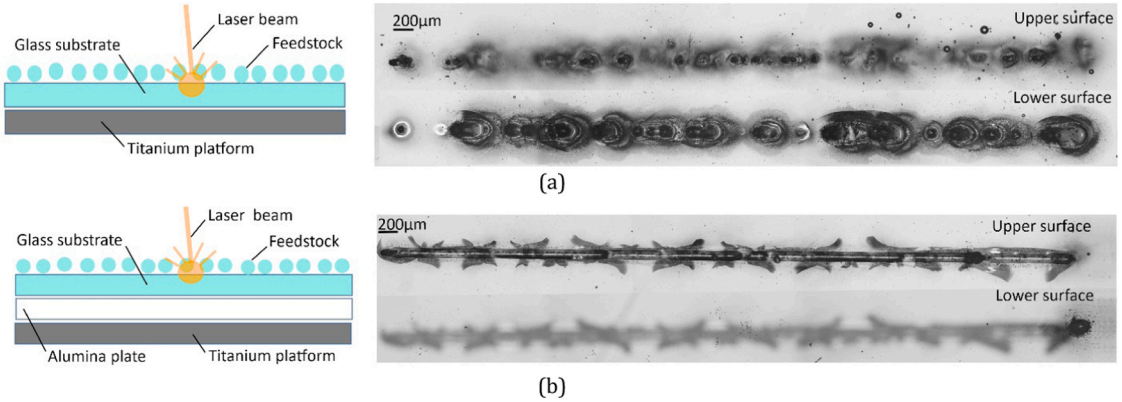

Fig. 3. Micrographs of the upper and lower surface of single scan tracks (SLSG109, 100 W and 37 mm/s) formed on a soda lime silica glass substrate that is fixed to (a) a titanium platform and (b) an alumina plate.

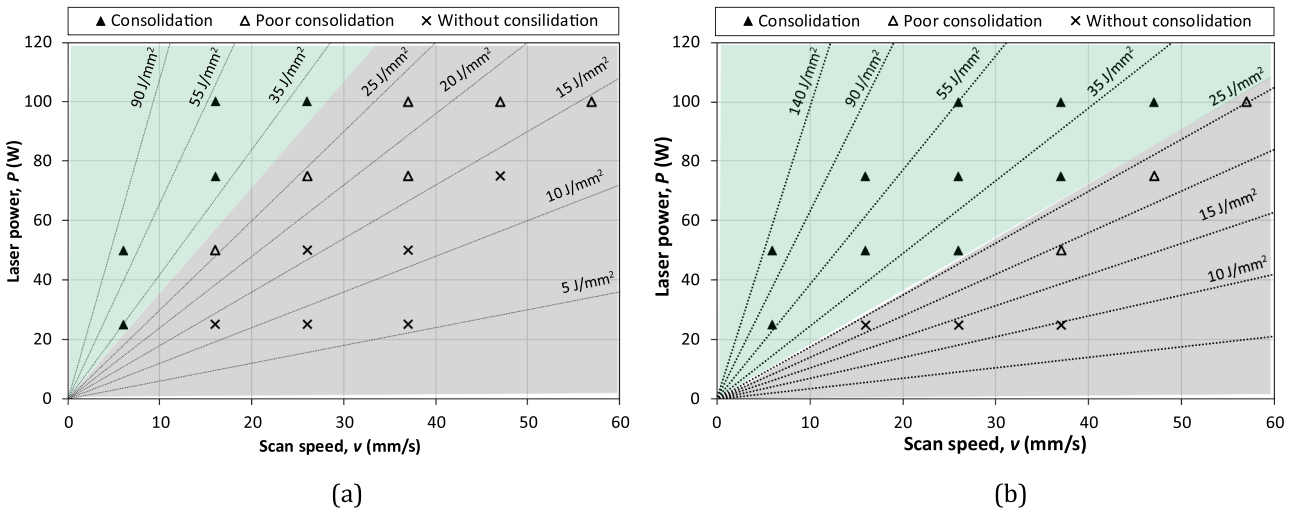

Fig. 5. Process maps for achieving consolidation in thin walled structures for: (a) SLSG109 and; (b) SLSG44 (green area for consolidated parts and grey area for poorly / unconsolidated parts).

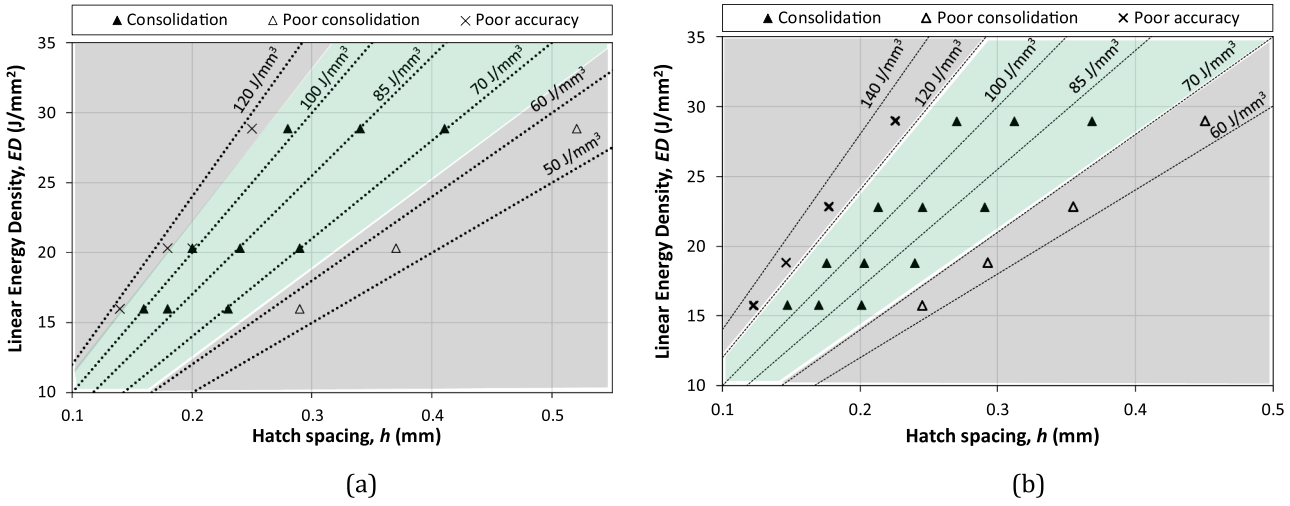

Fig. 6. Process maps for achieving consolidation in thick walled structures for: (a) SLSG109 and; (b) SLSG44 (green area for consolidated parts and grey area for poorly / unconsolidated parts or parts with excessive track height /poor accuracy).

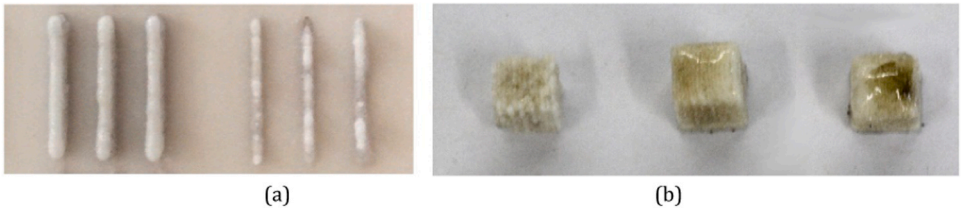

Fig. 7. LPBF of glass: (a) Thin walled structures showing good consolidation (left) and poor consolidation (right) and; (b) cubic structures showing poor consolidation (left), good consolidation (middle) and balling (right).

4.1. Continuous flow reactors (CFRs)

These typically involve a number of inlets that supply reactants at precise flow rates into a series of channels whose geometry is optimised for mixing and residence time of a particular chemical reaction.

LPBF of glass can be used for manufacturing CFRs offering the opportunity of customization in combination with the inertness of glass. These can be manufactured either in the form of a ready-to-use reactor or as individual channels that can be integrated in modular CFR systems in combination with conventional fittings. Examples of flow reactor channels in various geometries are provided as proof of concept in Fig. 9a-c. The partially fused powder particles on the surface of parts, manufactured with LPBF, could potentially provide an additional advantage for better mixing of reactants similar to the use of baffles in conventional CFRs.

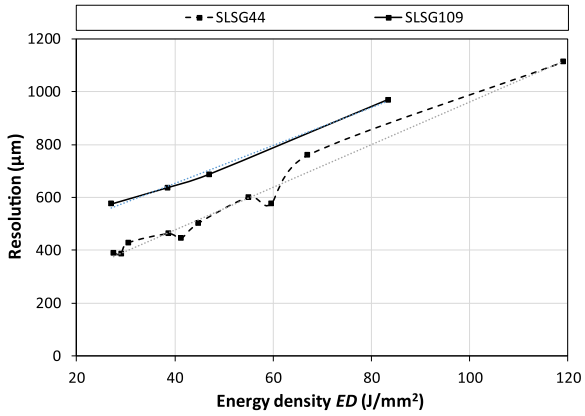

Fig. 8. Resolution for thin walled parts as a function of the selected energy density for both feedstock.

4.2. Monolithic structured catalysts

these are found in shapes of grid meshes, micro-channel reactors or even lattices. LPBF of glass provides an opportunity to create complex geometries of high resolution that can be used as structured catalysts, without any pre-requisite for moulds. Customization is a major advantage of AM as the structured catalyst geometry can be tailor-made to increase the surface area, and be subsequently functionalized with the catalytically active material to suit the varying requirements for different chemical manufacturing processes. Examples of glass geometries produced through LPBF that can be potentially used as structured catalysts are presented in Fig. 10a-c. The presence of superficial, partially fused powder particles can provide an additional increase to the available surface area and improve the efficiency of the catalyst.

LPBF of glass can be a cost-efficient alternative to conventional manufacturing technologies for applications such as the above i.e. highly customized and intended for prototyping or manufacturing in limited production volumes. LPBF can overcome additional costs associated with conventional manufacturing methods such as: (a) the fabrication of moulds in glass casting processes or: (b) the long lead times for subtractive manufacturing processes (micromachining, laser ablation or etching, typically used for CFRs), whilst achieving a faster turnaround. However, and similar to other AM processes [10], the cost advantage of LPBF diminishes compared to conventional casting processes as the production volume increases, because additional costs for mould fabrication can be absorbed in the numerous manufactured parts.

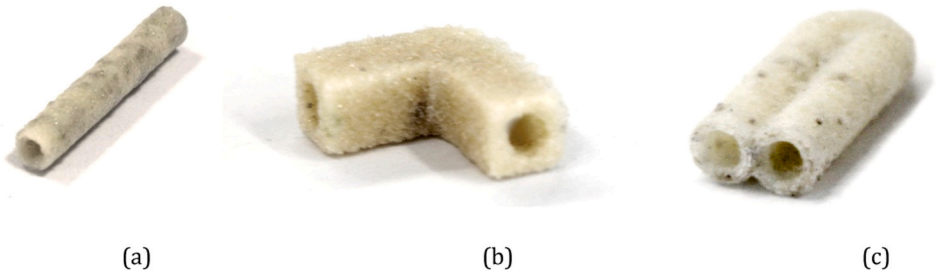

Fig. 9. Continuous flow reactor channels: (a) linear cylindrical channel (10 mm length and 2 mm internal diameter), (b) angle channel (12.5 mm length/side and 3 mm diameter) and (c) U-shaped channel (10 mm length and 2 mm internal diameter).

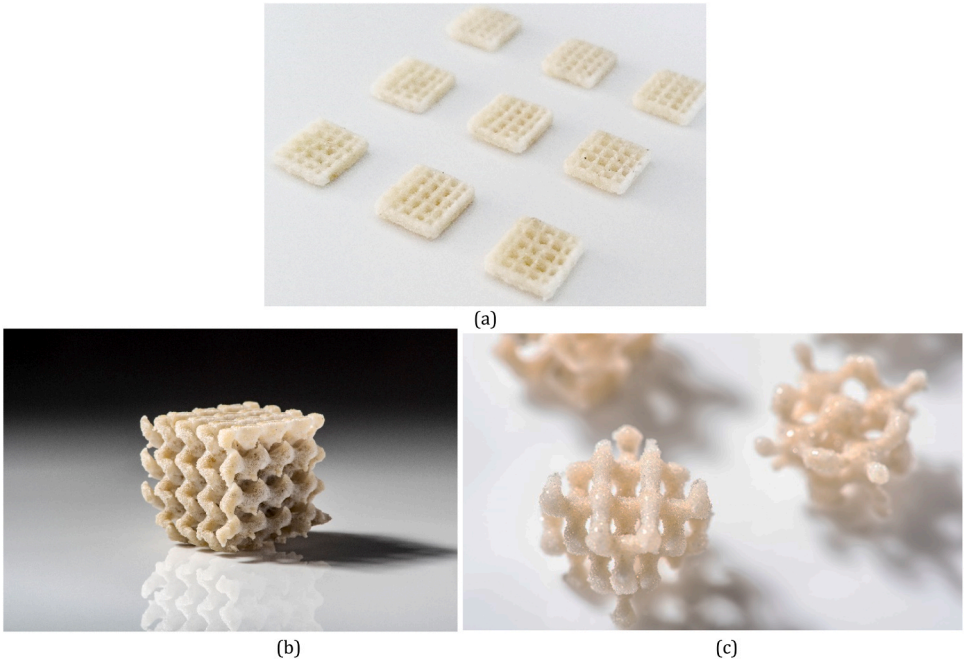

Fig. 10. Structured catalyst examples: (a) grid shaped rectangles ($7 \times 7 \times 1$ mm^3), (b) Gyroid network lattice ($20 \times 20 \times 20$ m^3), and (c) diamond network and BCC lattices ($10 \times 10 \times 10$ mm^3).

5. Physical and mechanical property evaluation methods

This section presents the evaluation methods for determining design limits, porosity, crystallinity and flexural strength in parts manufactured with LPBF of glass.

5.1. Geometrical limits

LPBF of linear, hollow cylindrical channels similar to channels used in a continuous flow reactor, was undertaken using SLSG-44, for geometrical optimisation (Fig. 9a). This involved investigation of design limits, taking into account wall thickness, internal diameter and channel length for straight channels with circular cross sections. A total of 72 combinations of design parameters were considered; designed wall thickness (t_w) ranged between $0.2 \leq t_w \leq 0.4$ mm in increments of 0.1 mm while designed internal diameter (D_{in}) and length (L) ranged between $0.5 \leq D_{in} \leq 2.0$ mm in increments of 0.3 mm and $5 \leq L \leq 14$ mm in increments of 3 mm respectively. Optical microscopy was also undertaken to determine the difference between designed and actual geometries.

5.2. Defects and porosity

The porosity and defects in built parts manufactured with LPBF and SLSG44 were investigated with micro-computed tomography (CT, ZEISS, XRADIA Versa XRM– 500, Germany). In particular two 5×5x5 mm^3 cubic samples, manufactured using the bounds of the optimal processing window in Fig. 6b (i.e. 79 and 108 J/mm^3), were evaluated. X-ray radiation provided cross sectional information on internal features based on the distribution of the X-ray attenuation coefficient. The output was 8-bit grayscale images, whose pixels were characterised by a grey-scale intensity factor (between 0 and 255). CT slices were obtained at a resolution of 4 μm through the thickness of the cubic samples. The images were subsequently processed through a Java script in the open source software ImageJ [11] to determine their porosity (steps shown in Fig. 11). The first step involved binarisation i.e. pixel conversion to black "0" and white "1" using an image segmentation algorithm that distinguishes pores from the glass structure. Following image segmentation, ImageJ automatically calculated the porous and total cross-sectional areas. The ratio of the former over the latter provided the sample porosity per slice.

A threshold is typically required in image segmentation to classify greyscale pixels in black or white. Multiple thresholding methods are available in literature and they are highly sensitive to the type of application and data [12]. Otsu's thresholding algorithm [13] was selected in this study as it was found to behave reliably for CT slices of glass beads in [14] and for non-destructive testing images in [12]. Clustering methods separate pixels in foreground and background classes by approximating the histogram with two Gaussian distributions. Otsu's method [13] defines threshold values by minimizing the within-class variance for foreground and background classes or equivalently by maximizing their between-class variance. Even though locally adaptive thresholding methods exist and can make separate segmentation decisions for each pixel based on its neighbouring pixels increasing its reliability, they are very computationally intensive. Additionally, they often depend on initial thresholding values or require manual supervision from the controller. For these reasons, they were not considered in this study.

5.3. Crystallinity

The molecular structure of the two cubic samples used above were additionally evaluated with X-ray diffraction (Bruker, D8 ADVANCE, USA) to determine whether the amorphous structure of the glass beads was maintained after laser processing.

5.4. Flexural strength

Glass is a brittle material lacking the ability to yield and redistribute stress. Therefore, any flaw is a potential stress concentration point that can propagate and lead to fracture when subjected to a certain level of tension. Assessing the flexural or tensile strength of glass consequently becomes critical. Typically, flexural tests are preferred for glass, as they prevent issues of misalignment and failure at the gripping locations that are commonly associated with tensile tests of brittle materials.

Three point bending (3PB) tests were therefore used to determine the flexural strength of prismatic specimens in a custom-made, miniature creep rig [15] (Fig. 12a-b). Four series of 24 samples with dimensions of 1×2x8 mm^3 were manufactured with LPBF and SLSG44 perpendicular to their longest axis (z). Three series involved linear scans along the short axis of the cross section (x) and energy densities of 79, 93 and 108 J/mm^3 while the fourth involved linear scans along the long axis of the cross section (y) and had an energy density of 108 J/mm^3 (Table 4). All samples were annealed for two hours at 560 ℃ (heating and cooling rate of 2 ℃/min) prior to mechanical testing to relieve any residual stress following the recommendation of [16]. The support span of the 3PB set-up was 5.35 mm while the strain rate was 0.0005 s^{-1}. The failure stress was subsequently calculated with Eq. 2:

$$\sigma_f = (3 \cdot P_f \cdot l_s)/(2 \cdot b \cdot d^2) \quad (2)$$

where P_f is the failure load, l_s= 5.35 mm, b= 2 mm and d= 1 mm are the support span, the width and the height of the prism respectively.

Glass is sensitive to subcritical crack growth when tested in non-inert conditions. Sub-critical crack growth is typically normalised for specimens failing at different times by converting the failure stress of each specimen to a time-equivalent strength [17]. To achieve this, the ramp stress history of the 3PB test was converted to a constant stress for a reference time period of t_{ref}= 60 s using Brown's integral [18] in Eq. 3.

$$\int_0^{t_f} \sigma_f^n(t)dt = \int_0^{t_{ref}} \sigma_{f,t_{ref}}^n dt \quad (3)$$

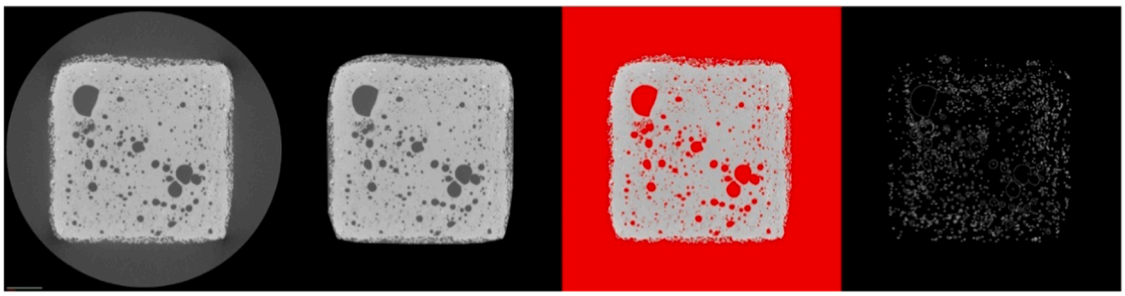

(a) (b) (c) (d)

Fig. 11. Porosity analysis procedure: (a) micro-CT slice of glass cube, (b) background removal, (c) image segmentation and (d) pore extraction.

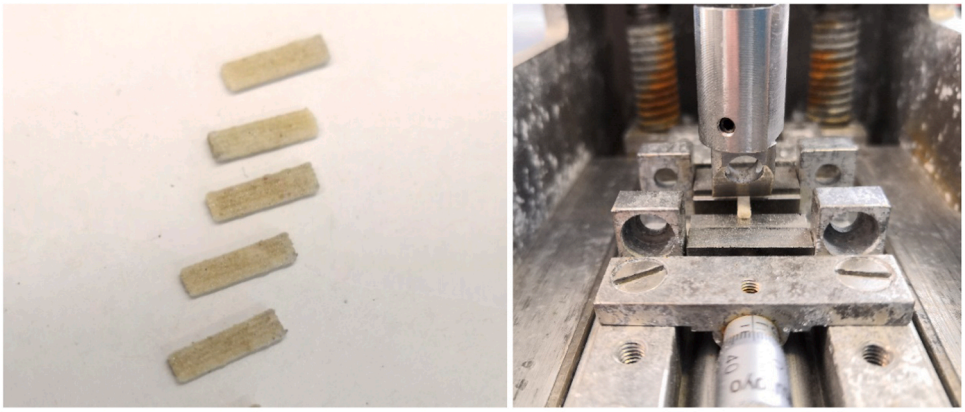

(a) (b)

Fig. 12. 3-point bending: (a) samples and (b) set-up.

Table 2
Design limits for flow reactor channels produced with LPBF.

Design limits	Wall thickness, t_w		
	0.2 mm	0.3 mm	0.4 mm
Minimum internal design diameter, D_{in}(mm)	1.1	1.7	2.0
Maximum length, L (mm)	14	14	8

Table 3
Dimensional accuracy for wall thickness results.

Designed Wall thickness t_w (μm)	Measured Features	Results (μm)	% diff
200	Max wall thickness $t_{w,max}$	688.5	244.2
	Min wall thickness $t_{w,min}$	533.1	166.6
	Mean wall thickness $t_{w,mean}$	619.6	209.8
	Standard deviation	51.4	
	Coefficient of variation cv %	8.3	
300	Max wall thickness $t_{w,max}$	1080.4	260.1
	Min wall thickness $t_{w,min}$	901.4	200.5
	Mean wall thickness $t_{w,mean}$	978.8	226.3
	Standard deviation	78.7	
	Coefficient of variation cv %	8.0	
400	Max wall thickness $t_{w,max}$	1247.6	211.9
	Min wall thickness $t_{w,min}$	1076.8	169.2
	Mean wall thickness $t_{w,mean}$	1168.0	192.0
	Standard deviation	94.2	
	Coefficient of variation cv %	8.1	

Table 4
Porosity of cubic samples produced with LPBF of SLSG44 with the max and min energy densities of the processing window.

Energy density	Mean porosity	Maximum porosity	Minimum porosity	Standard deviation	Coefficient of variation
J/mm^3	%	%	%		%
79	12.1	23.5	7.4	3.8	31.4
108	11.3	15.8	5.5	2.5	22.4

where t_f is the time to failure, $\sigma_{f,60}$ is the failure stress at the reference time period and n is the static fatigue constant ($n = 16$ for soda lime silica glass and common laboratory conditions [19]).

The results were statistically analysed and fitted to a 2-parameter Weibull distribution (Eq. 4) following the recommendations and procedure outlined for weighted least squares regression of glass strength data in [19].

$$P_f = 1 - \exp\left(-\left(\frac{\sigma_{f,60}}{\theta}\right)^{\beta}\right) \quad (4)$$

where P_f is the probability of failure while β and θ are the shape and scale factor of the Weibull distribution respectively.

6. Results and discussion

6.1. Geometrical limits

The minimum permissible design diameter and length were investigated with varying wall thickness (Table 2). Design lengths up to 14 mm could be achieved without cracking when a design wall thickness of 0.2 mm was used whilst the maximum permissible design length diminished to 8 mm when the design wall thickness increased to 0.4 mm. The length limitation in thicker channels was attributed to the larger energy input that was deposited per layer. Larger energy inputs created areas of accumulated heat (observed as bright orange areas during manufacturing), increased temperature gradients in built parts and led to the development of thermal stress and eventually cracking.

Channels with thinner walls also permitted smaller internal diameters to be manufactured; hollow cross sections could be achieved down to internal design diameters of $D_{in} = 1.1$ mm for a $t_w = 0.2$ mm whilst this increased to $D_{in} = 1.7$ mm for $t_w = 0.4$ mm. Internal design diameters below this limit resulted in solid instead of hollow cross sections. The heat-affected zone led to partial fusion of particles that were located adjacent to its edges, creating differences between design and manufactured dimensions, often inhibiting powder removal and justifying why solid cross-sections are found when small internal design diameters were selected. These particles could not be removed without post-processing (e.g. acid etching) and they limited dimensional accuracy. However, in some cases they might be useful in CFR applications as they add turbulence, creating vortices in the flow and improve mixing, similar to the action of baffles in a CFR.

Dimensional accuracy was further investigated with optical microscopy. It was found that the outer diameters, D_{out} and the wall thicknesses increased while the internal diameters decreased in all channels from design to manufacture. A mean increase of about 200% was found for all wall thicknesses with the actual mean thickness being $t_{w,actual} = 620$ μm for $t_w = 200$ μm, $t_{w,actual} = 979$ μm for $t_w = 300$ μm and $t_{w,actual} = 1168$ μm for $t_w = 400$ μm (Table 3). The mean increase in outer diameter ranged between 17.5% and 19.7% and the mean decrease in internal diameter ranged between 34% and 46%.

Despite the significant offset between design and manufactured dimensions, the above differences were quite consistent for all samples. Therefore, they could potentially be taken into account during the design stage of a CFR to predict its actual dimensions or vice versa to

calculate the required design dimensions to achieve the desired manufactured ones.

6.2. Defects and porosity

Micro-CT revealed three types of defect randomly distributed throughout the sample (Fig. 13a): (a) pores, (b) areas containing un-sintered powder particles and (c) cracks. The pores were fully enclosed and not interconnected, which is advantageous for solid-walled continuous flow reactor applications to ensure leak tightness. Cracks were mostly found near the lower surface of the specimen, i.e. closer to the substrate, and are attributed to the temperature gradients and the thermal stress that were developed during the manufacturing process, also observed in the LPBF of ceramics [20]. Increasing the temperature of the substrate beyond 250 °C and just below the transition temperature of the selected glass feedstock, is expected to reduce thermal cracking. Finally, areas containing un-sintered powder particles were mostly found near the top surface of the cubes. Layers further away from the top surface were exposed to a larger number of laser scans since part of the unabsorbed laser irradiation travelled through the glass sample and re-processed previous layers consolidating any powder particles that had been left intact from previous scans. This would indicate that a final surface scan could be used to reduce this defect.

Additionally, semi-fused powder particles, also known as "satellites", that adhere to the surface of the structure, were also noticed. The presence of "satellites" in combination with internal defects are responsible for the opaque appearance of the glass. Again, a final surface scan could potentially be used to change the topology of the surface, however, it should be noted that in some applications, such as chemical reactors, a rough surface can be advantageous in mixing.

Analysis of the micro-CT slices with ImageJ revealed a mean porosity of 12% for the 79 J/mm^3 sample, which was marginally higher than the 11% mean porosity for the 108 J/mm^3 sample. However, the porosity fluctuated considerably within the samples (Fig. 13b) due to the random distribution of the flaw, with 31.4% coefficient of variation for the 79 J/mm^3 sample and 22.4% for the 108 J/mm^3 sample. The results are summarised in Table 4.

6.3. Crystallinity

XRD results (Fig. 14) confirmed that no crystallisation was induced/produced during the LPBF process and that the samples remained completely amorphous for the two bounds of the optimal processing window (79 and 108 J/mm^3).

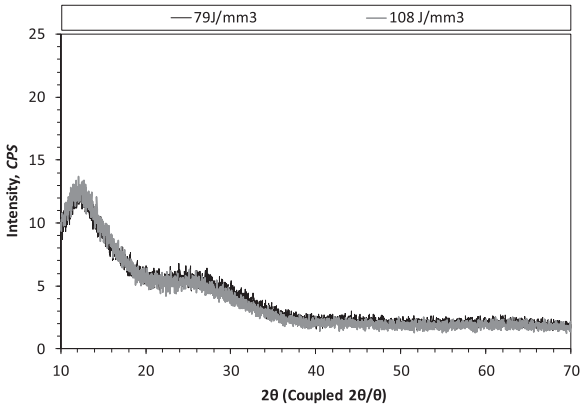

Fig. 14. X-ray diffraction of cubic samples produced with LPBF of SLSG44 with the max and min energy densities of the processing window.

6.4. Flexural strength

Good fit to the Weibull distribution was observed for all series (Table 5). Very similar values were found for the shape factor of the Weibull distribution that defines the slope of the cumulative distribution function and for strengths at mean (P_f=50%) and design (P_f=0.008, ASTM 1300–16 [21]) levels (Fig. 15a) for series 108x and 108y. This showed that the direction of the laser processing, i.e. scans parallel to the short (x) or the long (y) axis of the rectangular cross section, do not influence the flexural strength. Mean strengths (P_f=50%) also remained similar when different energy densities were used (79x, 93x, 108x) and ranged between 6.23 and 6.90 MPa. However, this did not apply for failure strengths at low probabilities of failure, e.g. the design strength was 1.76 MPa for 108x, followed by 2.96 MPa for 79x and by 3.78 MPa for 92x. The higher coefficient of variation in the 108x series led to a shallower slope in the cumulative distribution function justifying this larger discrepancy in the low probabilities of failure that could arise from different types of origins of failure (e.g. in Fig. 13a). The flexural

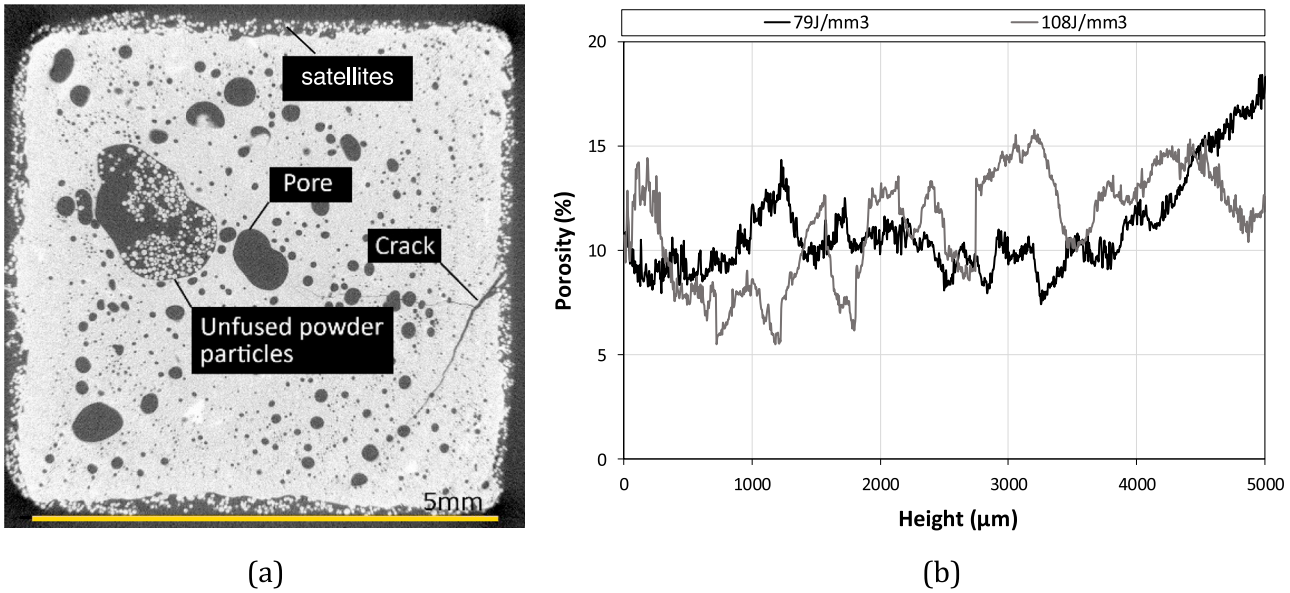

Fig. 13. Porosity and defects in glass LPBF built parts: (a) CT slice of glass cube containing typical defects (pores, cracks and unfused powder particles) and (b) Fluctuation of porosity through cubic sample as a function of its height.

Table 5
Weibull statistics for prismatic glass LPBF samples.

Series			Weibull parameters			Fractile values			
Energy density	Hatch direction	Shape factor	Scale factor	Goodness of fit	Coef. of variation	Design strength	Min stress	Max stress	Mean strength
ED		β	θ	p_{AD}	*CV*	$\sigma_{f,0.008}$	min σ_f	max σ_f	$\sigma_{f,0.50}$
J/mm^3	x/y		MPa	%	%	MPa	MPa	MPa	MPa
79	x	5.98	6.63	7.20	19.42	2.96	2.71	8.98	6.23
93	x	7.43	7.24	15.09	15.90	3.78	2.64	9.08	6.90
108	x	3.48	7.02	34.01	31.79	1.76	2.30	9.10	6.32
108	y	3.35	7.49	57.32	32.96	1.77	3.90	11.02	6.71

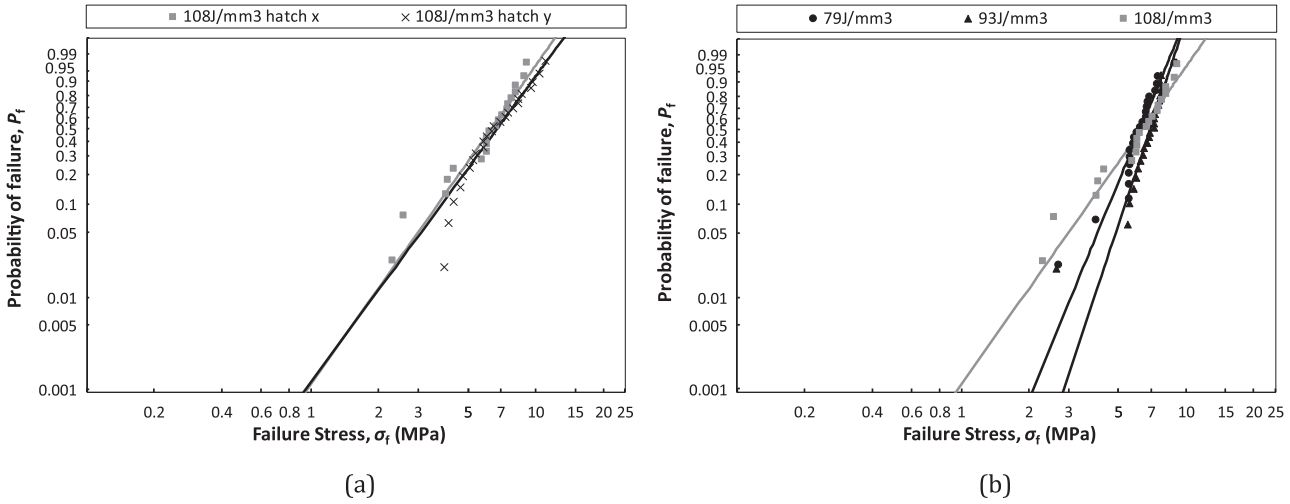

Fig. 15. Cumulative distribution functions for glass strength data of prismatic glass LPBF samples manufactured with varying: (a) direction of laser processing and (b) energy density.

strength of the additively manufactured parts was significantly lower than the strength of float soda lime silica glass (e.g. $\sigma_{f,0.008}$ =67.44 MPa $\sigma_{f,50}$ =108.5 MPa for as-received annealed glass [22]). This could be attributed to the high percentage porosity that created stress concentration points during testing within the built parts and triggered early fracture.

7. Conclusions

This paper has presented the optimisation of a laser powder bed fusion method for glass, evaluated the mechanical and physical properties of the manufactured parts and presented potential applications. Process maps were populated for two soda lime silica glass feedstock materials of different particle size, indicating that the optimal energy density window is independent of particle size when the composition remains largely the same. However, and unsurprisingly, resolution improved when finer feedstock was used as smaller layer thickness could be selected during the manufacturing stage.

Geometrical design limits were identified in linear hollow cylindrical channels with different features. Limitations in dimensional accuracy were noted due to partially fused powder particles that adhere to the surface walls. This is a common issue with powder bed fusion and can usually be improved with optimised scan strategies or post-processing techniques [23,24]. Also, the offset between manufactured and design limits can potentially be taken in account during the design stage. Porosity in the built parts marginally exceeded 10% and appeared in the form of fully enclosed pores while the mean flexural strength ranged between 6.2 and 6.9 MPa.

Potential uses of this technology were identified in the chemical manufacturing and pharmaceutical industries, in particular in continuous flow reactor and structure catalysts applications where the chemical inertness of glass surpasses the need for transparency. The presence of partially fused powder particles on the walls could be beneficial in such applications as they improve mixing of reactants in continuous flow reactors or increase the surface area in structured catalysts. Additionally, the presence of porosity is not expected to affect their performance as pores were found to be fully enclosed indicating that a leak tight performance is possible for continuous flow reactors. Even though the mean flexural strength of the additively manufactured parts was found to be significantly lower than standard float glass, this is expected to be sufficient for low pressure applications.

Further optimisation should be undertaken at a manufacturing level to reduce porosity and improve mechanical properties potentially building on previous research on ceramics [20]. Additionally, the influence of processing parameters on the geometrical performance of manufactured parts should be investigated and potentially assessed using geometrical benchmark artifacts [25]. Further testing should be also undertaken at a feasibility level to assess the performance of an additively manufactured structured catalysts and / or continuous flow reactors under real laboratory conditions and for a particular chemical manufacturing process. However, and despite its limitations, this is the first study that actively evaluated the properties of LPBF of glass and proposed potential applications, providing the stepping stone for future optimisation and development of the technology.

CRediT authorship contribution statement

K.C. Datsiou: Investigation, Writing - original draft. **F. Spirrett:** Investigation, Writing - review & editing. **I. Ashcroft:** Conceptualization, Writing - review & editing, Supervision. **M. Magallanes:** Conceptualization; Writing - review & editing, Funding acquisition. **S. Christie:** Writing - review & editing, Funding acquisition. **R.Goodridge:** Conceptualization, Writing - review & editing, Supervision, Funding acquisition.

Declaration of Competing Interest

The authors declare that they have no known competing financial interests or personal relationships that could have appeared to influence the work reported in this paper.

Acknowledgements

Financial support from Innovate UK (project number 103447) and the Engineering and Physical Sciences Research Council (grant number EP/P027261/1) is gratefully acknowledged. The authors would also like to thank Davide De Focatis for training and allowing access to the miniature creep rig in the Polymer Engineering Research lab for mechanical testing and Mark Hardy for his technical support during experimental parts of this work.

References

[1] F. Kotz, K. Arnold, W. Bauer, D. Schild, N. Keller, K. Sachsenheimer, T.M. Nargang, C. Richter, D. Helmer, B.E. Rapp, Three-dimensional printing of transparent fused silica glass, Nature vol. 544 (7650) (2017) 337–339.
[2] D.T. Nguyen, C. Meyers, T.D. Yee, N.A. Dudukovic, J.F. Destino, C. Zhu, E.B. Duoss, T.F. Baumann, T. Suratwala, J.E. Smay, R. Dylla-Spears, 3D-printed transparent glass, Adv. Mater. 29 (26) (2017) 1–5.
[3] J.F. Destino, N.A. Dudukovic, M.A. Johnson, D.T. Nguyen, T.D. Yee, G.C. Egan, A. M. Sawvel, W.A. Steele, T.F. Baumann, E.B. Duoss, T. Suratwala, R. Dylla-Spears, 3D printed optical quality silica and silica – titania glasses from sol – gel feedstocks, Adv. Mater. Technol. 3 (1700323) (2018) 1–10.
[4] J. Klein, Additive Manufacturing of Optically Transparent Glass (Master's Thesis), Massachusetts Institute of Technology, USA, 2015.
[5] A. Bracha and E. Gal-Or, 3D Printing system for printing high melting temperature materials, WO/2018/163006, 2018.
[6] K.C. Datsiou, E. Saleh, F. Spirrett, R. Goodridge, I. Ashcroft, D. Eustice, Additive manufacturing of glass with laser powder bed fusion, J. Am. Ceram. Soc. 102 (2019) 4410–4414.
[7] M. Fateri, A. Gebhardt, Selective laser melting of soda-lime glass powder, Int. J. Appl. Ceram. Technol. 12 (1) (2015) 53–61.
[8] R.D. Goodridge et al., Indirect selective laser sintering of an apatite–mullite glass–ceramic for potential use in bone replacement applications, Proc. IMechE, vol. 220 Part H: J. Engineering in Medicine, 2006.
[9] S. Ziegelmeier, P. Christou, F. Wöllecke, C. Tuck, R. Goodridge, R. Hague, E. Krampe, E. Wintermantel, An experimental study into the effects of bulk and flow behaviour of laser sintering polymer powders on resulting part properties, J. Mater. Process. Technol. 215 (2015) 239–250.
[10] E. Atzeni, A. Salmi, Economics of additive manufacturing for end-usable metal parts, Int. J. Adv Manuf. Technol. 62 (2012) 1147–1155.
[11] W. Rasband, "ImageJ." https://imagej.nih.gov/ij, 1997–2018, National Institutes of Health, Bethesda, Maryland, USA.
[12] M. Sezgin, B. Sankur, Survey over image thresholding techniques and quantitative performance evaluation, J. Electron. Imaging 13 (1) (2004) 146–168.
[13] N. Otsu, A threshold selection method from gray-level histograms, IEEE Trans. Syst. Man Cybern. SMC-9 (1) (1979) 62–66.
[14] P. Iassonov, T. Gebrenegus, M. Tuller, Segmentation of X-ray computed tomography images of porous materials: a crucial step for characterization and quantitative analysis of pore structures, Water Resour. Res. 45 (9) (2009) 1–12.
[15] D. De Focatis, P. Buckley, Determination of craze initiation stress in very small polymer specimens, Polym. Test. 27 (2008) 136–145.
[16] T. El-Sayed, R.J. Hand, Modelling the strengthening of glass using epoxy based coatings, J. Eur. Ceram. Soc. 31 (2011) 2783–2791.
[17] M. Haldimann, Fracture strength of structural glass elements - analytical and numerical modelling, testing and design (PhD Thesis), École Polytechnique Fédérale de Lausanne, Switzerland, 2006.
[18] W.G. Brown, A load duration theory for glass design, Ottawa, 1972.
[19] K.C. Datsiou, M. Overend, Weibull parameter estimation and goodness-of-fit for glass strength data, Struct. Saf. 73 (2018) 29–41.
[20] S.L. Sing, W.Y. Yeong, F.E. Wiria, B.Y. Tay, Z. Zhao, L. Zhao, Z. Tian, S. Yang, Direct selective laser sintering and melting of ceramics: a review, Rapid Prototyp. J. 23 (is. 3) (2017) 611–623.
[21] ASTM, "Standard Practice forDetermining Load Resistance of Glass in Buildings. ASTM Standard E1300–16," ASTM Int., pp. 1–62, 2016.
[22] K.C. Datsiou, M. Overend, Artificial ageing of glass with sand abrasion, Constr. Build. Mater. 142 (2017) 536–551.
[23] J. Vaithilingam, R.D. Goodridge, R. Hague, S. Christie, S. Edmondson, The effect of laser remelting on the surface chemistry of Ti6al4V components fabricated by selective laser melting, J. Mater. Process Technol. 232 (2016) 1–8.
[24] Kruth, J. et al., "Part and material properties in selective laser melting of metals", 16th Int Symposium on Electromachining (ISEM), pp. 1–12, 2010.
[25] L. Rebaioli, I. Fassi, A review on benchmark artifacts for evaluating the geometrical performance of additive manufacturing processes, Int J. Adv. Manuf. Technol. 93 (2017) 2571–2598.